Received: 20 June 2020 | Revised: 13 October 2020 | Accepted: 10 November 2020

DOI: 10.1111/jmi.12980

Journal of Microscopy RMS

ORIGINAL ARTICLE

Phase determination in dual phase steels via HREBSD-based tetragonality mapping

Derrik Adams[1] | **Michael P. Miles**[1] | **Eric R. Homer**[1] | **Tyson Brown**[2] | **Raj K. Mishra**[2] | **David T. Fullwood**[1]

[1] Department of Mechanical Engineering, Brigham Young University, Provo, Utah

[2] General Motors Corp, Detroit, Michigan

Correspondence
David T. Fullwood, Department of Mechanical Engineering, Brigham Young University, Provo, UT 84602.
Email: dfullwood@byu.edu

Abstract

Electron Backscatter Diffraction (EBSD) is a widely used approach for characterising the microstructure of various materials. However, it is difficult to accurately distinguish similar (body centred cubic and body centred tetragonal, with small tetragonality) phases in steels using standard EBSD software. One method to tackle the problem of phase distinction is to measure the tetragonality of the phases, which can be done using simulated patterns and cross-correlation techniques to detect distortion away from a perfectly cubic crystal lattice. However, small errors in the determination of microscope geometry (the so-called pattern or projection centre) can cause significant errors in tetragonality measurement and lead to erroneous results. This paper utilises a new approach for accurate pattern centre determination via a strain minimisation routine across a large number of grains in dual phase steels. Tetragonality maps are then produced and used to identify phase and estimate local carbon content. The technique is implemented using both kinetically simulated and dynamically simulated patterns to determine their relative accuracy. Tetragonality maps, and subsequent phase maps, based on dynamically simulated patterns in a point-by-point and grain average comparison are found to consistently produce more precise and accurate results, with close to 90% accuracy for grain phase identification, when compared with an image-quality identification method. The error in tetragonality measurements appears to be of the order of 1%, thus producing a commensurate ~0.2% error in carbon content estimation. Such an error makes the technique unsuitable for estimation of total carbon content of most commercial steels, which often have carbon levels below 0.1%. However, even in the DP steel for this study (0.1 wt.% carbon) it can be used to map carbon in regions with higher accumulation (such as in martensite with nonhomogeneous carbon content).

KEYWORDS
body-centred tetragonal (BCT), dual phase (DP) steel, electron backscatter diffraction (EBSD), electropolish, image quality (IQ), pattern/projection centre (PC), tetragonality

1 | INTRODUCTION

The development of steels with higher strength and formability has accelerated over the past few decades, in order to deliver improved performance with less material. The resultant alloys are key to lightweighting strategies of vehicle manufacturers, where downgauging leads to lighter vehicles and higher fuel efficiency. Advanced high-strength steels (AHSS) are created using complex thermomechanical processes that result in intricate blends of hard and soft phases, in order to deliver both strength and formability. The continued discovery and optimisation of enhanced steels depends, in large part, on the ability to characterise these complex structures, including mapping out the various phases present. Body centred tetragonal (BCT) martensite differs from body centred cubic (BCC) ferrite in that is has a tetragonal lattice induced by interstitial carbon atoms; tetragonality is essentially a stretch in the *c*-axis, manifest as a small eigenstrain. Common methods for distinguishing between the phases generally rely upon differences in their properties (such as hardness; see the review below), rather than quantifying the level of tetragonality which is the basis for the difference in behaviour.

This paper applies high-resolution electron backscatter diffraction (HREBSD), using simulated reference patterns, to dual phase (DP) steel in order to map the tetragonality of the crystal lattice, and thereby distinguish the BCC and BCT phases, as well as estimate the local carbon content from the determined *c*-to-*a* ratio.

DP steels obtain their desirable high strength-to-formability ratio through a composite-like microstructure composed of ferrite and martensite phases.[1] While the percentage of the two phases varies depending on the type of DP steel, it is typical to have DP steels with martensite phase fractions ranging from 30% to 50%,[2–4] where the characteristics of the martensite phase, specifically carbon content, related tetragonality and morphology, play a key role in the mechanical properties.[5–7] The average carbon content within the martensite will vary, most directly with the overall carbon concentration in the alloy and the martensite volume fraction; however, various studies have also shown that the carbon content within a region of martensite can vary significantly. In one case study with overall carbon concentration of 0.18%, the average carbon content in the grains was typically 0.3-0.4 wt%C, but there was a significant gradient of carbon within the martensite region depending upon the prior heat treatment (for example, reaching around 0.5% carbon).[8] Another study developed a new technique to map carbon content, and demonstrated large variations across the martensite substructure. The DP steel had an overall carbon content of 0.15%, and carbon content within a martensite grain varied from negligible content to around 0.7%.[9]

Common methods of distinguishing the ferrite and martensite phases within steel depend upon characteristics such as their hardness, level of internal disorder (eg dislocation content that interferes with diffraction quality), or reaction to chemical etchants. Colour etchants, such as LePera etching, reveal the phases by colouring them differently.[10,11] Another common etchant used is nital. While it does not colour the grains in the same manner as the LePera etch, the nital etch corrodes the phases at different rates, making them distinguishable via topography.[12] Subsequent image analysis is applied in order to interpret the surface features and extract phase fractions. Apart from the sometimes ambiguous phase interpretation, the process also changes the surface of the sample such that other characterisation techniques, such as electron backscatter diffraction (EBSD), are made more difficult or impossible. This generally precludes using EBSD on etched specimens, making it difficult to subsequently match phases with other key microstructure data like crystallographic orientation and grain morphology.

Nanoindentation is another method used to identify martensite within DP steels, since martensite and ferrite have different hardness properties.[1] However, both the spatial and hardness resolution obtained via nanoindentation can be limited; extremely small grains are more difficult to characterise, and local differences in orientation (and therefore, apparent hardness) can make the interpretation difficult. Additionally, the process deforms the sample surface, which also inhibits later characterisation techniques such as EBSD.

For many materials, dissimilar phases can be distinguished via EBSD itself.[13] Commercial EBSD software generally analyses a diffraction pattern from a scanning electron microscope and identifies the position of bands, that correspond with planes of atoms, using a Hough transform. By comparing the arrangement of band intersection points with those from a database, the software can categorise phase and orientation simultaneously for each scan point, if the correct phase was included in the list of potential phases by the user. The process of the software categorising the crystal structure and orientation is commonly termed ‘indexing’. However, while this approach works well for distinguishing obviously distinct phases (such as face centred cubic and BCC), the difference between BCC and BCT structures is often too subtle (i.e. when the level of tetragonality is low) and requires an accuracy of band detection by the software that is currently not available.

Other methods have been used to distinguish similar phases via EBSD. These include separating phases by grain size,[14,15] band slope values,[16] Confidence Index (CI) values, Image Quality (IQ),[17–19] kernel average misorientation[20]

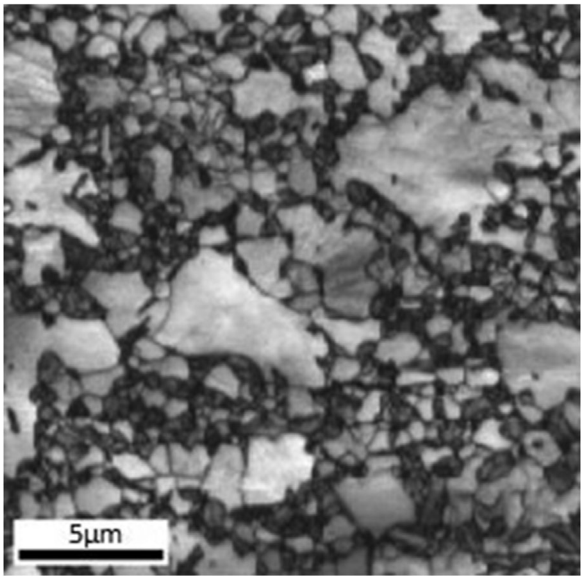

FIGURE 1 Image quality map of DP steel. Dark regions correspond to low IQ, often indicating martensite. Brighter regions correspond to higher IQ which is more typical of ferrite

or similar metrics specific to the particular commercial EBSD software being used. For steel alloys, IQ is often used to distinguish martensite and ferrite. It quantifies the contrast or clarity of EBSD images in terms of the intensities of Hough peaks, relating to the crystal lattice planes. These values are then mapped to a greyscale image, which provides, to some extent, a map of lattice disorder across the sample (see Figure 1). Because martensite typically has a higher dislocation content than ferrite,[21] it will produce poorer patterns and therefore have a lower IQ value, appearing as darker regions within the IQ map. While this method is widely accepted as providing a reasonable estimate of the correct phase, it has some drawbacks. In particular, image quality is susceptible to factors other than dislocation content in phases. Surface finish, scan parameters (which can vary from one scan to the next), surface debris etc.,[18,19] can all adversely affect image quality. One cannot be certain if an area of low image quality is due to a particular phase or something else entirely.

Recent work has also utilised dynamically simulated patterns as references for distinguishing similar phases.[22-25] The patterns reproduce the band profiles of real patterns much more accurately than kinematically simulated patterns. For example, the method by Ram et al.[23] compares the real patterns to a dictionary of simulated patterns that could exist for that phase, and computes a similarity metric for each comparison. The final phase is then the phase for which the similarity metric is highest, indicating the phase and the real pattern are the most similar. For multi-phase materials, each pattern is matched against dictionary patterns for each of the probable phases. As reported, better than 86% accuracy was obtained when using this approach, and for FCC phases with differences in lattice constants greater than 12%, an accuracy of 100% was obtained.

The current paper uses a method related to that presented by Ram et al,[23] in that simulated patterns (both kinematically and dynamically simulated in our case) are compared with real patterns in order to differentiate the BCC from the BCT phase. However, rather than just looking at some measure of goodness of fit, the actual tetragonality of the lattice is quantified using cross-correlation techniques for more detailed information regarding the BCT phase (an idea conceived in Ref. 26).

The underlying method for determining tetragonality has been demonstrated for 'perfect' silicon/SiGe crystals using both kinematically simulated[27] (Figure 2c shows an example kinematically simulated pattern for bcc iron) and dynamically simulated patterns[28] (Figure 2b illustrates a dynamically simulated pattern for iron). Furthermore, a similar approach was tested for resolving pseudosymmetry in lathe TiAl.[29] However, the low image quality typically associated with EBSD of martensite presents a particularly challenging hurdle for a method that relies upon high-fidelity patterns for distinguishing slight band shifts. Furthermore, a critical issue relating to the comparison of simulated patterns for determination of lattice strain involves the accurate determination of microscope geometry (the 'pattern centre' or 'projection centre', PC) that must be accurately reflected in the pattern simulations. Small errors in the PC can lead to 'phantom strains', which cause significant error in the tetragonality measurements.[26,30]

The PC indicates the position of the electron emission point on the sample, relative to the phosphor screen reference frame.[27] It is defined by x^*, y^* and z^* Cartesian coordinates that are typically given as percentages of the phosphor screen width or diameter. Various estimates of pattern centre accuracy have been given for different fitting algorithms;[29–31] for example, in some cases it appears that standard commercial EBSD software can achieve an accuracy of around 0.5% using standard working conditions, which should result in a tetragonality error of around 0.5% (figure 6 of Ref. 26). However, these estimates of PC accuracy are likely made on materials that produce high-quality patterns. Several references agree that a PC error of less than 0.5% is needed to reduce phantom strain levels to the order of 10^{-3};[26,30,32] this is the order of magnitude of resolution desired in order to distinguish martensite from ferrite phases.

A range of methods for more accurate PC calibration have been previously proposed. These include shadow casting,[33] iterative fitting,[34] screen moving,[32] calibrating from a single crystal with known structure and lattice constant,[34,35] and mapping Kikuchi bands onto a sphere.[31]

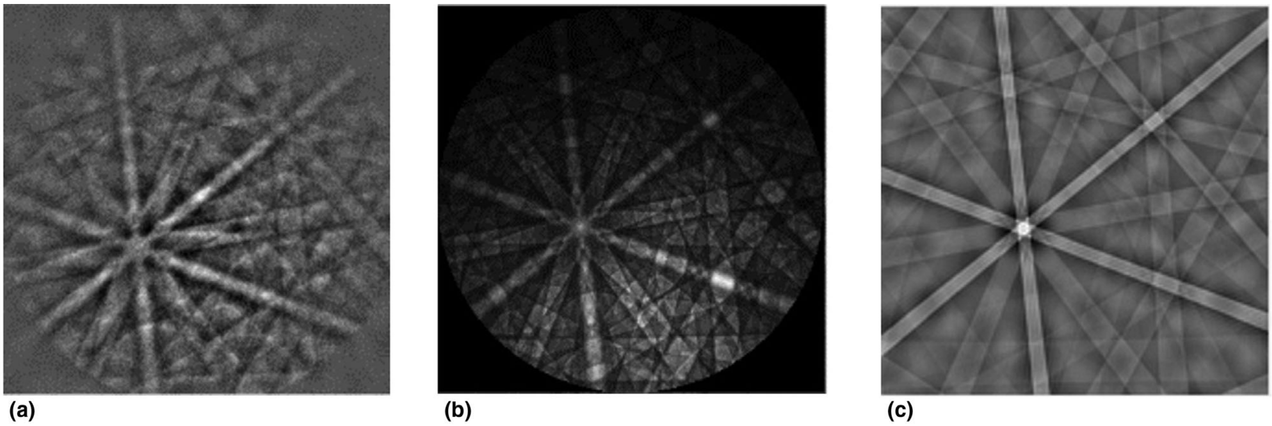

FIGURE 2 Example Kikuchi patterns used for PC calibration of DP 980 sample. (a) Actual EBSD pattern, (b) dynamically simulated pattern, (c) kinematically simulated pattern

Each of these methods provide calibrated PC's to varying levels of accuracy but often require more information than that available in a regular set of EBSD patterns. In this paper, a new PC calibration approach is presented, inspired by previous strain minimisation approaches,[26,27] but adapted to work in polycrystalline samples with nonzero lattice strain, and variable pattern quality.

The resultant maps of tetragonality for DP steel are compared with SEM images of the etched topography and IQ maps of the same sample. The related phase fraction estimates are assessed relative to expected values, and carbon content is inferred and compared with manufacturer's data.

2 | METHODS

2.1 | Material and data acquisition

The material used in this study was a DP 980 steel obtained from US Steel, Pittsburgh, PA, USA, with a nominal composition of 0.1% C, 0.15% Si, and 2.35% Mn. While the detailed processing conditions are typically confidential for commercial steels, thermomechanical processing of DP 980 steel starts with austenitising of the material, then reducing the temperature to an appropriate intercritical level, in order to achieve the desired portions of ferrite and austenite.[36] After intercritical annealing the material is water quenched, resulting in a microstructure with about 50% volume fraction of martensite for the current steel.[37]

Sample preparation for EBSD consisted of mechanically polishing to 1200-fine and then applying a final electropolish. The electrolyte used consisted of 125 mL Methanol, 75 mL Butanol and 25 mL Perchloric acid, which was kept at approximately 10 C. The samples were electropolished at 20V and 1.1 A for 24 seconds. EBSD scans were taken in an Apreo C Low-Vac SEM. An accelerating voltage of 20KV, current of 3.2nA, and working distance of 20 mm were used, with a standard sample tilt of 70 degrees (see Ref. 38 ch 1). Patterns were collected by an EDAX Digiview camera at 1 × 1 binning with the default background subtract applied, and indexed using EDAX's OIM Data Collection 7.2 software (pattern images were 925 × 925 pixels). In both cases, EBSD patterns were saved for all points within a scan for later analysis.

2.2 | Tetragonality and pattern centre

Using Brigham Young University's open source cross-correlation software, OpenXY,[39] the PC for each sample was calibrated by effectively minimising the median lattice strain (relative to that of a cubic lattice) over many grains within the sample at the same time, as described below. As mentioned, PC errors cause phantom strains that would make patterns coming from a cubic lattice appear to be associated with a strained (noncubic) lattice. If the lattice is known to be cubic, with only small elastic strains (eg for the BCC ferrite phase), then varying the PC to minimise the apparent strain associated with the EBSD patterns will result in a correct PC position. This approach also works on a tetragonal lattice (ie with a nonzero pseudo strain, such as the martensite BCT lattice, which is assumed to be a distortion of the BCC phase) provided that patterns are taken from a distribution of grain orientations. This was tested using purely simulated patterns (with known tetragonality). While the minimisation of strain associated with the EBSD pattern for a single grain would result in the wrong PC (since the lattice is not cubic), the error is corrected by performing the strain minimisation over many grains (with different orientations). Figure 3 illustrates the effect using kinematically simulated reference patterns. In

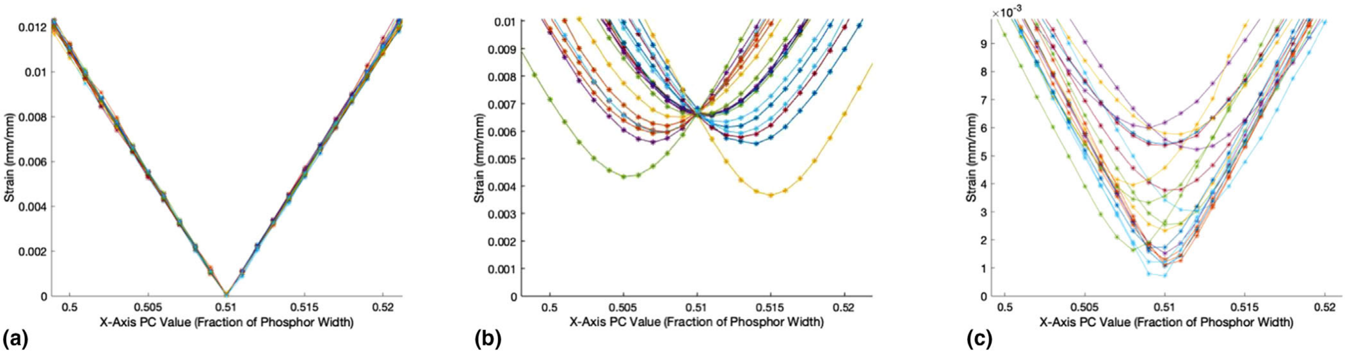

FIGURE 3 Apparent strain change with pattern centre variation for 20 random orientations, calculated using kinematically simulated reference patterns: (a) for BCC iron reference patterns, (b) for BCT reference patterns with a single tetragonality value of 1% and (c) for random BCT tetragonality values between 0 and 1%

Figure 3a, 20 random orientations are selected, and a reference BCC iron EBSD pattern is simulated. The simulated PC value for *x* is 0.51. The *x* value of PC is then varied and the OpenXY software calculates the (phantom) equivalent elastic strain associated with the PC error. Different orientations result in similar behaviour for strain versus PC error, having a distinct minimum point (that of the correct PC). In Figure 3b, randomly oriented BCT reference patterns are simulated, each with a constant tetragonality value of 1%, and the exercise is repeated. In this case, the minimum strain for each random orientation occurs at a different PC, but these values are centred on the correct PC. In Figure 3c, random orientations and tetragonality values (between 0 and 1%) are selected for each reference pattern. The aggregated minimum strain value across the PC range is clearly at the correct position of 0.51.

Trials on different areas of the steel, and on sets of simulated EBSD patterns with different orientations (but consistent tetragonality), indicated that at least 20 different points in the sample should be chosen, ideally across a wide range of orientations, for best results. For this study, > 50 points were selected on an evenly-spaced grid. The procedure is described in detail in Ref. 28 Starting from the estimated value of PC derived by the commercial EBSD software, the lattice distortion relative to a cubic lattice is calculated for each of these points (after adjusting the PC for each geometrical position). To determine the distortion, simulated pattern is created, the distortion of the real pattern relative to the simulated pattern is calculated, and any orientation discrepency between simulated and real pattern is corrected by simulating a new pattern in an iterative manner for the default value of 4 iterations, and then the lattice distortion is extracted from the measured shifts between features in the reference and experimental patterns. Dynamically simulated patterns were generated by EMSoft[40] (also described in Refs. 28,41). This process was repeated across the space of possible correct pattern centres. Initially x^* and y^* were held constant while the PC was varied across a range of z^* values on either side of the estimated value. After discarding strain values above a certain noise threshold (taken to be 0.5% strain in this study – the default value in OpenXY; as can be seen from Figure 4, this is well above the main population of measured strain values), a quadratic function was fit to the median value of strain for the remaining points (see Figure 4; the quadratic fit is not included in the plot, in order to more easily see the median value line). The location of the minimum indicates the correct value of z^*. The assumption that the correct PC is the one that, on average, minimises the strain across the sample by the simulated pattern method is discussed in more detail in the results section. This process is then repeated for y^* and then for x^*, using the updated values of the previously calibrated dimensions. The process is then repeated once more to converge on the accurate PC value. The order of calibration of the dimensions was chosen due to the typically higher sensitivity of calculated strain to the z^* value, leading to easier calibration.

The corrected PC was then fed into the relevant (ie kinematical or dynamical) pattern simulation routine, along with the estimated orientation from the EBSD software. The resultant simulated pattern was compared with the actual EBSD pattern arising from the given point on the sample using cross correlation analysis, as described in previous papers.[26,42] After adjusting the orientation based on the new PC, the relative lattice strain between the simulated and real patterns is quantified using the technique described in more detail in Refs. 27,28 Those strains are then used to measure the corresponding tetragonality based on the following equation[35]:

$$\varepsilon^{tetr} = \varepsilon_{33}^{crystal} - \frac{\varepsilon_{11}^{crystal} + \varepsilon_{22}^{crystal}}{2}, \tag{1}$$

where ε^{tetr} is the tetragonality as a function of the major axis strains of the crystal lattice. For the martensite BCT phase, the *c*-axis is assumed to align with the 3-direction,

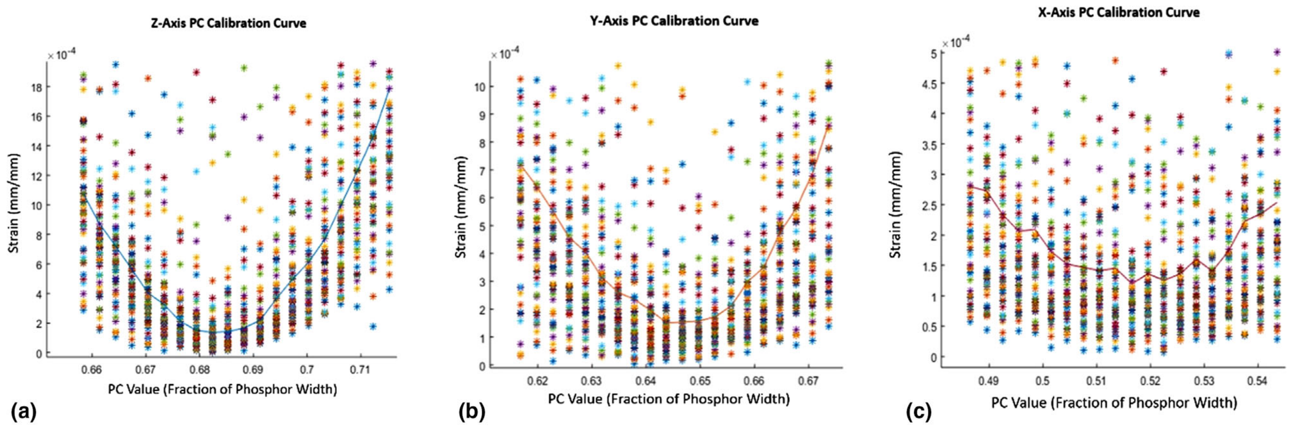

FIGURE 4 Strain calculated for a group of grains (each represented by a different colour dot) over a range of PC values. (a)-(c) Strain values when varying *Z*, *Y* and *X* values of PC, respectively, while holding the other values constant; the solid lines indicate the median value

and the *a* and *b* lattice parameters are assumed to be consistent with those of the bcc phase. Hence, $\varepsilon_{11}^{crystal} = \varepsilon_{22}^{crystal} = 0$, and $\varepsilon_{33}^{crystal} = (c-a)/a$; that is ${}^{c}/_{a} = 1 + \varepsilon^{tetr}$.

Note that for the kinematically simulated patterns, the tetragonality of the simulated lattice is adjusted until the real and simulated patterns match, according to the cross-correlation (see Ref. 27). For the dynamically simulated patterns, this would be computationally inefficient (the ‘master pattern’ would need to be regenerated for each level of tetagonality, at high computational cost[43]). However, if a cubic lattice is assumed, and the measured value of tetragonality is above around 2%, the error in the measured value becomes significant due to the widening difference between the reference and experimental patterns. Hence, master patterns of dynamically simulated patterns were generated at different levels of tetragonality (0%, 2%, 4% and 6%), and the best fit pattern (after searching over the three possible *c*-axis directions) was used as the reference pattern for a given point; the final tetragonality is given by that of the reference pattern plus the measured distortion from that value.

Expected tetragonality levels were determined based on the nominal composition of the DP steel used in this study, which contained approximately 0.1 wt% C. Actual carbon content within the martensite phase can vary significantly across a grain or colony as noted in Ref. 9 (and as can be seen in figures later in this paper). These variations cause the tetragonality (*c*/*a* ratio) to vary approximately linearly according to carbon content based on the following equation.[35, 44, 45]

$$ {}^{c}/_{a} = 1 + 0.045 \times \text{wt\%C} \quad \text{i.e.} \quad \varepsilon^{tetr} = 0.045 \times \text{wt\%C}. \tag{2} $$

2.3 | Phase identification baseline

For the DP steel in this study, IQ maps provide a good differentiator between martensite and ferrite regions. Figure 5 includes IQ and SEM secondary electron images of two regions of the steel, selected to illustrate two levels of morphological complexity. The electrolyte used during the electropolishing step slightly etched the sample surface, helping to highlight the two phases, with the softer ferrite undergoing a deeper etch, generally. While the beam, sample and detector geometry lead to differences in the clarity of topographical features, depending upon orientation of the features, the higher regions in the SEM images generally coincide with the darker martensite areas that are apparent in the IQ maps. This provides some verification of the phase distinguishing capability of the IQ approach for this material. We note that while the topography has a slight effect on the pattern centre *z*-value discussed above, the very light electropolishing etch only changes the surface height by nanometres, and hence does not have a significant affect at the target levels of resolution discussed. Furthermore, there is not a significant effect on pattern quality (such as measured from the confidence index).

The threshold for distinguishing between ferrite and martensite in the IQ map was selected by plotting the histogram of IQ values, and selecting the point corresponding to the end of the initial low IQ peak (Figure 6). This peak is assumed to correlate with regions of martensite. Since both areas in this study used the same microscope settings, and had the same range of IQ values, the same threshold of 30,000 was used in both cases. The resulting martensite area fraction identified by points having IQ below this value agrees with the fraction of martensite expected for this material (~50%), as will be apparent below.

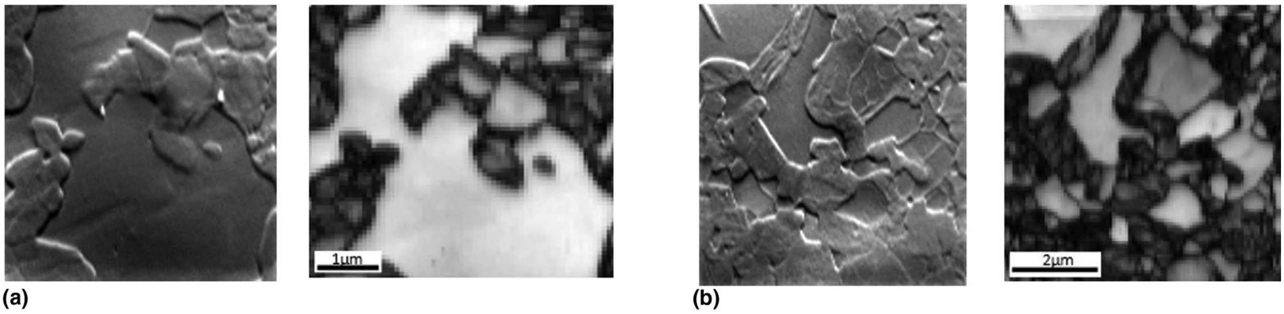

FIGURE 5 (a) (Left) SEM image of etched Area 1. Raised regions correspond to martensite. (Right) IQ map of same area. (b) (Left) SEM image of etched Area 2. (Right) IQ map of same area

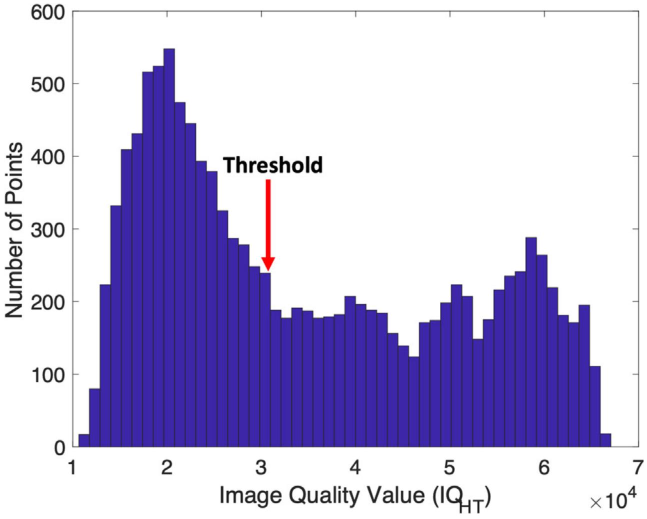

FIGURE 6 Joint histogram of IQ values from Areas 1 and 2, indicating the threshold for distinguishing martensite (below the threshold) from ferrite (above the threshold)

3 | RESULTS AND DISCUSSION

3.1 | PC calibration

As previously mentioned, a PC with target error of less than 0.5% (of phosphor screen width) is sought, to sufficiently reduce the phantom strains that might cause significant errors in tetragonality measurements. Based upon the curve of median values in Figure 4, it appears that a clear minimum for each axis can be identified within ~0.005 (as a fraction of the phosphor width). Note that, as discussed in the method section, the sensitivity of the method is different in different directions; the curvature of the median value line is significantly lower for the *x*-dimension (Figure 4c) compared with the other dimensions. Nevertheless, when a quadratic is fit to the data, identification of the minimum to within ~0.005 is feasible. Thus, it seems reasonable to expect that the error of the new PC value is adequate to achieve the desired resolution of 0.5%.

Several further activities were undertaken to test this hypothesis. First, BCT dynamically simulated patterns (with the same parameters used for the steel comparison) with a known tetragonality (0.4%) were created over a random set of orientations, and with known PC. Using the approach described above, the PC that minimised the median effective strain across the set of orientations was determined, and found to be closer than 0.1% from the correct value. This confirmed that by minimising strain over a random set of orientations, the PC can be found, even if the lattice strain is not zero, at least for the case of perfect patterns without noise. In a typical material, the tetragonality will vary; but if enough points are taken to sample a range of orientations for a given level of tetragonality, an accurate PC should be found by this approach. In a series of tests on simulated patterns, minimising elastic strain across a minimum of around 20 randomly sampled grains resulted in convergence to the stated 0.1% from correct PC of the simulation.

Figure 7a demonstrates a tetragonality map (Equation 1) of a dual phase steel using the best available PC from the commercial software. In this case, the tetragonality calculated for ferrite grains with different orientations differs greatly. This highlights the fact that the approximately linear relationship between PC error and a given strain component (such as the strain along the *c*-axis) is highly dependent upon the orientation. In addition, the PC error for this material must be around 4% in order to give the observed tetragonality error – much higher than the estimates above (this assumes that the actual level of tetragonality in the ferrite grains, as identified by Figures 7b and c, is negligible). Note that once the PC has been corrected (Figure 7b), using the method in this paper, the tetragonality in the ferrite grains is less than about 0.2%. Based upon the estimates of phantom strain error in Ref. 35, figure 6, the levels of tetragonality measured in the ferrite (which should have zero tetragonality) in Figure 7b indicate that the PC error is

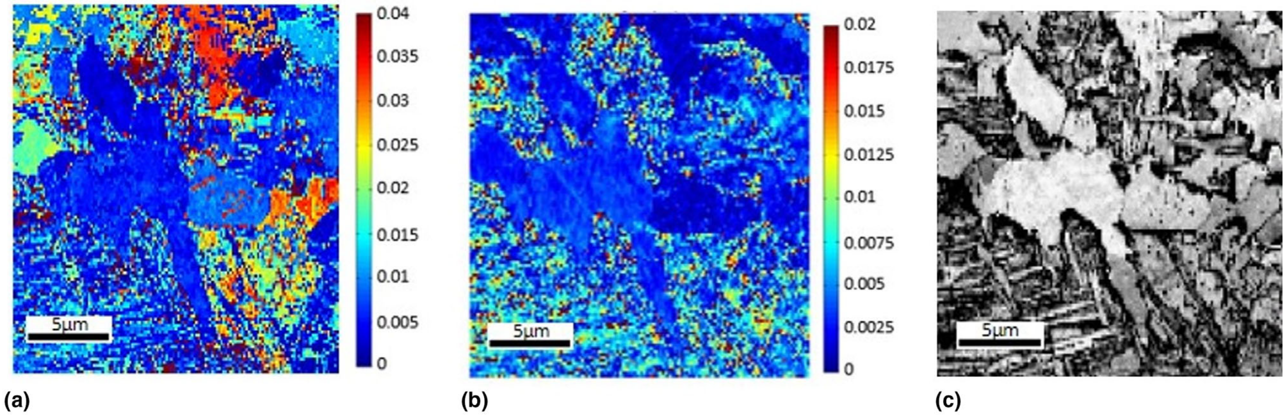

FIGURE 7 (a) Original tetragonality map for dual phase steel, with PC taken from commercial EBSD software. (b) Tetragonality map with recalibrated PC using the method in this paper. (c) Image quality (IQ) map for the sample, indicating ferrite (high IQ areas) and martensite (low IQ regions)

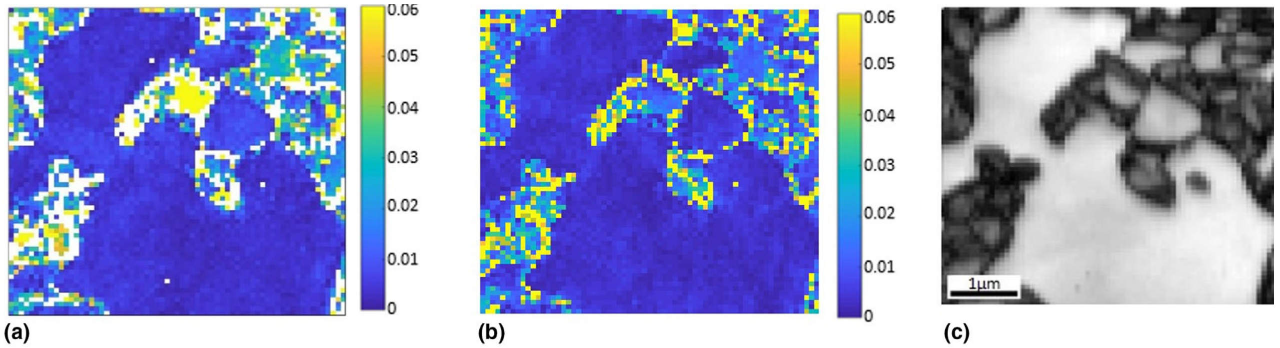

FIGURE 8 Area 1 maps: (a) Tetragonality map (equals $c/a - 1$, or $0.045 \times$ tarpon content) made using kinematically simulated patterns (b) Tetragonality map made using dynamically simulated patterns; white pixels in these images have not converged to a reliable answer in HREBSD. (c) IQ Map of corresponding scan, where dark regions are presumably martensite and light areas are ferrite

around 0.2% for that particular sample. As a further verification, nine individual areas of the DP steel were analysed independently, and the PC for each area was calculated using the current approach. The precision in PC (the standard deviation between the calculated values, based upon the assumption that the microscope correctly determined the correct distance between the analysed areas) was better than 0.4%.

3.2 | Tetragonality maps

Tetragonality maps were created from two separate EBSD scans of 5×5 μm (Area 1) and 6.5×6.5 μm (Area 2) areas, at an EBSD step size of 75 nm. Two different analyses were undertaken for each scan area, using kinematically and dynamically simulated patterns for cross-correlation, respectively. For either case, the experimental pattern from the steel must be indexable by the EBSD software to provide the correct orientation for simulating the initial reference pattern. While martensite is notorious for having poor pattern quality, the polishing method described above resulted in indexable points across the entire scans. There may be a potential for lower fidelity at grain boundaries due to pattern mixing, but that does not appear to have caused a strong effect in the resultant tetragonality maps. Figures 8 and 9 show the tetragonality maps resulting from both approaches for each scan, compared to the corresponding IQ map. In both cases, the suspected ferrite grains (lighter regions on the IQ map) have tetragonality close to 0%, as expected. Therefore, the main difference between the kinematic and dynamic approaches occurs within the martensite regions. Note that points with suspect results (poor convergence of the cross correlation method, indicated by a summed-squared error, SSE, of greater than 25) are rejected and assigned a white colour on the map; they are not included in the averaging for grain tetragonality. This filtering only

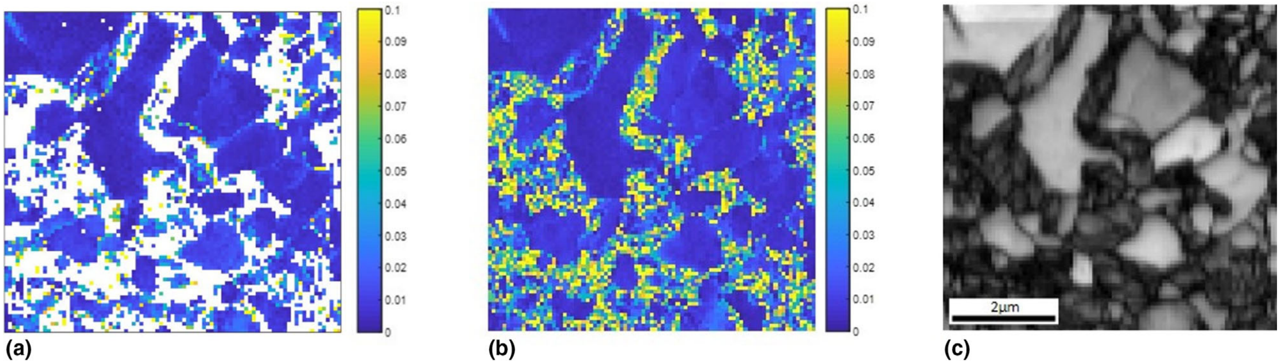

FIGURE 9 Area 2 maps: (a) Tetragonality map (equals $c/a - 1$, or 0.045 × wt.% carbon content) based on kinematic patterns. (b) Tetragonality map based on dynamic patterns; white pixels in these images have not converged to a reliable answer in HREBSD. (c) IQ Map of corresponding scan

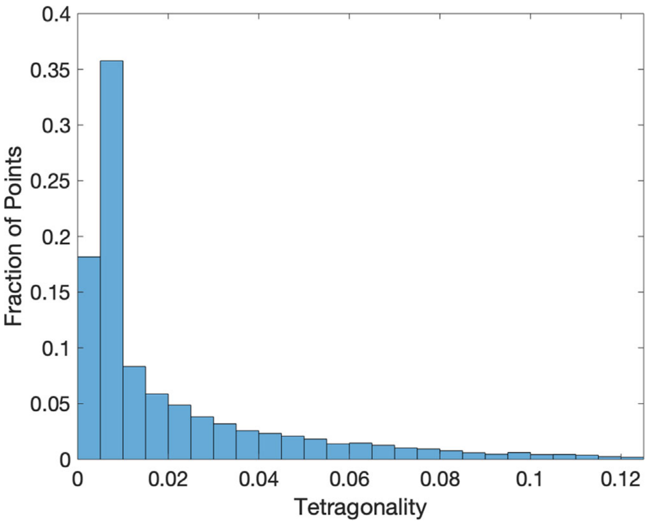

FIGURE 10 Histogram of tetragonality values (equals $c/a - 1$, or 0.045 × wt.% carbon content) determined by the dynamic reference pattern method for Area 1

applies to the kinematical results, where they constitute approximately 10% of the map; the suspect points also strongly correlate with points with confidence index, CI, as determined by the EBSD software, of less than 0.05. The dynamically simulated patterns produce a tetragonality map with no points having high SSE values.

To evaluate the difference between the kinematic and dynamic approaches, the resulting tetragonality maps were compared directly to the corresponding IQ maps via both a grain average and a point-by-point comparison. Points/grains with tetragonality > 1% ($c/a > 1.01$, carbon content > ∼0.2%) as determined by the HREBSD approach were assumed to be martensite; this value marks the edge of a peak on the distribution of tetragonality values calculated by HREBSD. Figure 10 shows the histogram of tetragonality values calculated for Area 1 using the dynamic pattern method. There is a clear transition at 0.01 tetragonality.

In the point-by-point comparison of martensite regions as determined by the tetragonality approach versus the IQ approach, dynamic simulation proved to have higher accuracy than kinematic for both areas scanned. Dynamic reference patterns resulted in an average accuracy of 83.2% (meaning that points with tetragonality values above 1% corresponded correctly with low IQ values for the same point), while kinematic simulation resulted in an average accuracy of 66.8%; these values are averaged across the two test areas. However, both methods identify tetragonality levels with higher accuracy when assigning individual grains to be either ferrite or martensite based on average tetragonality. Dynamic simulation resulted in an average accuracy of 89% (ie grains covering 89% of the total sample area were correctly assigned to the relevant phase, as identified by the IQ map), while kinematic had an average accuracy of 83.3%.

The performance of the dynamically simulated reference pattern method is also tabulated in Table 1 in terms of area fraction of martensite identified by the method, compared to IQ. As another distinguisher of martensite versus ferrite, a best fit metric is reported, where EBSD patterns that are closest to the cubic reference pattern (0% tetragonality) are assigned to be ferrite, and other points are assigned to be martensite. The average fraction of martensite identified by IQ (accounting for the difference in areas of the two regions) is 49%; the expected value is ∼50% (see also Refs. 2–4). While this is not a validation of the IQ approach, due to the approximate nature of the expected value, the small areas, and the imprecise method of selecting the IQ threshold, it nevertheless provides some assurance that the IQ metric provides a reasonable distinction between phases for this particular steel. The tetragonality metric indicates a slightly lower martensite content than IQ for both areas. Furthermore, the best

TABLE 1 Identification of martensite/ferrite for Areas 1 and 2

	Area 1			Area 2		
	Tetragonality metric	Best fit pattern metric	IQ metric	Tetragonality metric	Best fit pattern metric	IQ metric
Assumed ferrite (Tet. ≤1.0%, best fit pattern = 0%, or IQ ≥ 30k)	69.1%	71.7%	66.4%	45.0%	52.6%	41.4%
Assumed martensite (Tet. > 1.0%, best fit pattern > 0%, or IQ < 30 k)	30.9%	28.3%	33.6%	55.0%	47.4%	58.6%

fit pattern approach indicates even lower fractions of martensite, as would be expected since martensite with low levels of tetragonality would have EBSD patterns that are closer to the 0% tetragonal pattern than the 2% pattern.

One of the additional benefits to measuring tetragonality comes from the observed relationship between tetragonality and carbon content. With a known tetragonality value, approximate carbon content at a point can be calculated using Equation 2. We note that other factors relating to the processing history of the steel may affect the tetragonality,[46] and the detailed proprietary heat treatment is not known. If the raw tetragonality data is used to estimate carbon content, the minority of high tetragonal values (as indicated in the Figure 10 histogram) would dominate the results. If the points that align best with the 6% tetragonal simulated pattern are examined, these are predominantly single pixels, indicating that they are associated with noise. This is possibly due to poor indexing (ie initial estimation of their orientation), which then results in poor estimates of tetragonality. For practical purposes, any points with tetragonality greater than 0.04 ($c/a > 1.04$, carbon content > ∼0.9%) were assumed to be outliers and not included in the carbon average calculation (see Figure 10); this removed the top 10% of points in terms of tetragonality. Points identified as ferrite were assumed to have 0% carbon; then, using Equation 2, Area 1 has 0.11% carbon, and Area 2 has 0.19% carbon. This results in a carbon content that is somewhat higher than that reported by the manufacturer (0.1 wt%C) indicating that tetragonality is overestimated in the martensite (or that Eq. 2 is not accurate for this material). Given that the tetragonality levels measured in the assumed ferrite region are as high as 1%, this appears to be the typical magnitude of error using the current approach. Such an error, of 1% tetragonality, relates to ∼0.2 wt. % carbon, which is higher than the expected carbon content in this material. Hence improvements in dealing with the sources of noise in the cross correlation method (including the PC calibration) are needed to more accurately map carbon content in typical carbon steels. However, it is interesting to note that the higher tetragonality values (and related carbon content) near the grain boundaries in Figures 8 and 9 are consistent with observations in Ref. 8.

4 | CONCLUSIONS

Tetragonality maps were produced using cross-correlation based HR-EBSD in order to help distinguish BCC ferrite from BCT martensite in a DP steel, using both kinematically and dynamically produced reference patterns.

In order to attain the target 0.5% accuracy for the pattern centre of the microscope (and avoid the generation of phantom strains that confuse the tetragonality measurements), a new strain minimisation approach achieved the requirement for the material being studied. While the current study indicates that the PC optimisation method will work well for cubic materials, or for tetragonal materials with random textures, the accuracy of the method for highly textured tetragonal materials has not been assessed.

For the DP steel studied here, IQ maps generate high contrast between ferrite and martensite regions, providing a suitable baseline for verifying tetragonality mapping approaches. The volume fractions of martensite obtained from the IQ maps align reasonably with manufacturer measurements (obtained using XRD), although these comparisons depend upon threshold selection, and therefore only demonstrate accuracy within about 10% volume fraction. The low IQ areas also generally align with plateaus in SEM images of the etched material, providing further verification.

Tetragonality measurements from dynamically simulated reference patterns provide significantly better alignment with the IQ results than the kinematically simulated patterns. In a point-by-point comparison the different approaches gave 83.2% and 66.8% accuracy, respectively. When compared at the grain level (taking the average tetragonality across a grain as the basis for the comparison), they achieve 89% and 83.3% accuracy, respectively. The error in the tetragonality measurement is indicated by the fact that tetragonality values in the assumed ferrite regions were fairly evenly distributed between 0 and 1%. This may be related to some remaining PC error, along with initial estimates of lattice orientation provided by EBSD software.

A further indication of the resolution of the approach is provided by estimating the carbon content within the martensite, and comparing with manufacturer-provided values. If points in the tail of the tetragonality distribution are ignored as outliers (the single pixel points that associate with > 4% tetragonality), then the carbon content in the two area that were examined (low and high martensite contents) were 0.11% and 0.19% respectively, compared with a manufacturer declared value of 0.1%. This aligns with the tetragonality resolution as being approximately 1%, giving an average error in carbon content of around 0.2%.

Overall, the study demonstrates a promising method for determining an accurate pattern centre, analysing lattice tetragonality and identifying BCT versus BCC regions; the magnitude of error in carbon content estimation makes the technique unsuitable for estimating total carbon content of most commercial steels, which often have carbon levels below 0.1%. However, even in the DP steel for this study (0.1 wt.% carbon) it can be used to map carbon in regions with higher accumulation (such as in martensite with nonhomogeneous carbon content).

ACKNOWLEDGEMENT

This work was supported by the National Science Foundation grant # DMR 1507095 and CMMI 1926662.

ORCID

David T. Fullwood https://orcid.org/0000-0002-7486-3672

REFERENCES

1. Zhang, F., Ruimi, A., Wo, P. C., & Field, D. P. (2016). Morphology and distribution of martensite in dual phase (DP980) steel and its relation to the multiscale mechanical behavior. *Materials Science and Engineering A—Structural Materials Properties Microstructure and Processing*, *659*, 93–103.
2. Ch.Darabi, A., Chamani, H. R., Kadkhodapour, J., Anaraki, A. P., Alaie, A., & Ayatollahi, M. R. (2017). Micromechanical analysis of two heat-treated dual phase steels: DP800 and DP980. *Mechanics of Materials*, *110*, 68–83.
3. Kim, D.-K., Kim, E.-Y., Han, J., Woo, W., & Choi, S.-H. (2017). Effect of microstructural factors on void formation by ferrite/martensite interface decohesion in DP980 steel under uniaxial tension. *International Journal of Plasticity*, *94*, 3–23.
4. Krajewski, S., & Nowacki, J. (2014). Dual-phase steels microstructure and properties consideration based on artificial intelligence techniques. *Archives of Civil and Mechanical Engineering*, *14*(2), 278–286.
5. Chen, H.-C., & Cheng, G.-H. (1989). Effect of martensite strength on the tensile-strength of dual phase steels. *Journal of Materials Science*, *24*(6), 1991–1994.
6. Marder, A. R. (1982). Deformation characteristics of dual-phase steels. *Metallurgical Transactions A—Physical Metallurgy and Materials Science*, *13*(1), 85–92.
7. Pierman, A.-P., Bouaziz, O., Pardoen, T., Jacques, P. J., & Brassart, L. (2014). The influence of microstructure and composition on the plastic behaviour of dual-phase steels. *Acta Materialia*, *73*, 298–311.
8. Farivar, H., Richter, S., Hans, M., Schwedt, A., Prahl, U., & Bleck, W. (2018). Experimental quantification of carbon gradients in martensite and its multi-scale effects in a DP steel. *Materials Science and Engineering A—Structural Materials Properties Microstructure and Processing*, *718*, 250–259.
9. Yamashita, T., Tanaka, Y., Nagoshi, M., & Ishida, K. (2016). Novel technique to suppress hydrocarbon contamination for high accuracy determination of carbon content in steel by FE-EPMA. *Scientific Reports*, 6, 1–7. https://doi.org/10.1038/srep29825
10. Kang, J.-Y., Park, S.-J., Suh, D.-W., & Han, H. N. (2013). Estimation of phase fraction in dual phase steel using microscopic characterizations and dilatometric analysis. *Materials Characterization*, *84*, 205–215.

11. Lepera, F. S. (1979). Improved etching technique for the determination of percent martensite in high-strength dual-phase steels. *Metallography*, *12*(3), 263–268.
12. Angeli, J., Füreder, E. & Panholzer, M. (2006). Etching techniques for characterizing the phases of low-alloy dual-phase and TRIP steels. *Pract. Metall.*, *43*(10), 489–504.
13. Fullwood, D., Adams, B., Basinger, J., Ruggles, T., Khosravani, A., Sorensen, C., & Kacher, J. (2014). Microstructure detail extraction via EBSD: An overview. In Barabash Rozaliya & Gene Ice (Eds.), *Strain and dislocation gradients from diffraction: Spatially-resolved local structure and defects* (p. 405). London: Imperial College Press.
14. Kang, J.-Y., Kim, D. H., Baik, S.-I, Ahn, T. -H., Kim, Y.-W., Han, H. N., …Han, S. H. (2011). Phase analysis of steels by grain-averaged EBSD functions. *Isij International*, *51*(1), 130–136.
15. Zhao, H., Wynne, B. P., & Palmiere, E. J. (2017). A phase quantification method based on EBSD data for a continuously cooled microalloyed steel. *Materials Characterization*, *123*, 339–348.
16. Ryde, L. (2006). Application of EBSD to analysis of microstructures in commercial steels. *Materials Science and Technology*, *22*(11), 1297–1306.
17. Wilson, A. W., Madison, J. D., & Spanos, G. (2001). Determining phase volume fraction in steels by electron backscattered diffraction. *Scripta Materialia*, *45*(12), 1335–1340.
18. Wright, S. I., & Nowell, M. M. (2006). EBSD image quality mapping. *Microscopy and Microanalysis*, *12*, 72–84.
19. Wu, J., Wray, P. J., Garcia, C. I., Hua, M., & Deardo, A. J. (2005). Image quality analysis: A new method of characterizing microstructures. *Isij International*, *45*(2), 254–262.
20. Zaefferer, S., Romano, P., & Friedel, F. (2008). EBSD as a tool to identify and quantify bainite and ferrite in low-alloyed Al-TRIP steels. *Journal of Microscopy*, *3*, 499–508.
21. Satdarova, F. F. (2016). Dislocation structure of martensitic transformation in carbon steel. *Physics of Metals and Metallography*, *117*(4), 355–363.
22. Nolze, G., Winkelmann, A., & Boyle, A. P. (2016). Pattern matching approach to pseudosymmetry problems in electron backscatter diffraction. *Ultramicroscopy*, *160*, 146–154.
23. Ram, F., & De Graef, M. (2018). Phase differentiation by electron backscatter diffraction using the dictionary indexing approach. *Acta Materialia*, *144*, 352–364.
24. Tanaka, T., & Wilkinson, A. J. (2018). High angular resolution electron backscatter diffraction studies of tetragonality in Fe-C martensitic steels. *Microscopy and Microanalysis*, *24*(S1), 962–963.
25. Winkelmann, A., Nolze, G., Cios, G., & Tokarski, T. (2018). Mapping of local lattice parameter ratios by projective Kikuchi pattern matching. *Physical Review Materials*, *2*(12). 1–7.
26. Kacher, J., Landon, C., Adams, B. L., & Fullwood, D. (2009). Bragg's Law diffraction simulations for electron backscatter diffraction analysis. *Ultramicroscopy*, *109*(9), 1148–1156.
27. Fullwood, D., Vaudin, M., Daniels, C., Ruggles, T., & Wright, S. I. (2015). Validation of kinematically simulated pattern HR-EBSD for measuring absolute strains and lattice tetragonality. *Materials Characterization*, *107*, 270–277.
28. Jackson, B. E., Christensen, J. J., Singh, S., De Graef, M., Fullwood, D. T., Homer, E. R., & Wagoner, R. H. (2016). Performance of dynamically simulated reference patterns for cross-correlation electron backscatter diffraction. *Microscopy and Microanalysis*, *22*(4), 789–802.
29. Jackson, B., Fullwood, D., Christensen, J., & Wright, S. (2018). Resolving pseudosymmetry in gamma-TiAl using cross-correlation electron backscatter diffraction with dynamically simulated reference patterns. *Journal of Applied Crystallography*, *51*, 655–669.
30. Britton, T. B., Maurice, C., Fortunier, R., Driver, J. H., Day, A. P., Meaden, G., …Wilkinson, A. J. (2010). Factors affecting the accuracy of high resolution electron backscatter diffraction when using simulated patterns. *Ultramicroscopy*, *110*(12), 1443–1453.
31. Basinger, J., Fullwood, D., Kacher, J., & Adams, B. (2011). Pattern center determination in electron backscatter diffraction microscopy. *Microscopy and Microanalysis*, *17*(3), 330–340.
32. Maurice, C., Dzieciol, K., & Fortunier, R. (2011). A method for accurate localisation of EBSD pattern centres. *Ultramicroscopy*, *111*(2), 140–148.
33. Venables, J. A., & Bin-Jaya, R. (1977). Accurate microcrystallography using electron back-scattering patterns. *Philosophical magazine*, *35*(5), 1317–1332.
34. Zambaldi, C., Zaefferer, S., & Wright, S. I. (2009). Characterization of order domains in gamma-TiAl by orientation microscopy based on electron backscatter diffraction. *Journal of Applied Crystallography*, *42*, 1092–1101.
35. Kacher, J. (2009). Cross-correlation-based texture analysis using kinematically simulated EBSD patterns. Provo: Brigham Young University, *xv*, 83.
36. Arruda, M. V. P., Melo, T. M. F., Costa, F. S., & Santos, D. B. (2019). Microstructural evolution during continuous annealing of a 980 MPa cold rolled steel grade. *Journal of Physics: Conference Series*, *1270*, 012020.
37. Ruggles, T., Cluff, S., Miles, M., Fullwood, D., Daniels, C., Avila, A., & Chen, M. (2016). Ductility of advanced high strength steel in the presence of a sheared edge. *Journal of the Minerals Metals and Materials Society*, *68*(7), 1839–1849.
38. Schwartz, A.J., Kumar, M., Adams, B. L., & Field, D. P. (eds.) (2009). *Electron backscatter diffraction in materials science*, 2nd ed. New York: Springer.
39. BYU, O. X. Y. (2017). Retrieved from https://github.com/BYU-MicrostructureOfMaterials/OpenXY.
40. De Graef, M. (2015). EMSoft 3.0. Retrieved from http://www.github.com/marcdegraef/emsoft.
41. Jackson, B., Christensen, J. J., Singh, S., De Graef , M., Fullwood, D. T., Homer E. R., & Wagoner, R. H. (2016). Performance of dynamically simulated reference patterns for cross correlation EBSD. *Microscopy & Microanalysis*, *22*(4), 789–802.
42. Wilkinson, A. J., Meaden, G., & Dingley, D. J. (2006). High-resolution elastic strain measurement from electron backscatter diffraction patterns: New levels of sensitivity. *Ultramicroscopy*, *106*(4–5), 307–313.
43. Callahan, P. G., & De Graef, M. (2013). Dynamical electron backscatter diffraction patterns. Part I: Pattern simulations. *Microscopy and Microanalysis*, *19*(5), 1255–1265.

44. Honeycomb, R., & Bhadeshia, H. (1995). *Steels, microstructure and properties, metallurgy and materials science*. London, England: Edward Arnold Butterworth Heinemann.
45. Roberts, C. S. (1953). Effect of carbon on the volume fractions and lattice parameters of retained austenite and martensite. *Transactions AIME*, *197*, 203–204.
46. Bhadeshia, H. K. D. H., & Honeycombe, R. W. K. (2006). *Steels microstructure and properties*. Oxford: Butterworth-Heinemann.

How to cite this article: Adams D, Miles MP, Homer ER, Brown T, Mishra RK, Fullwood DT. Phase determination in dual phase steels via HREBSD-based tetragonality mapping. *J. Microsc*. 2021;282:60–72. https://doi.org/10.1111/jmi.12980